Characterisation of the porous structure of Gilsocarbon graphite using pycnometry, cyclic porosimetry and void-network modeling

Giuliano M. Laudone[a], Christopher M. Gribble[a], G. Peter Matthews[a,*]

[a]*School of Geography, Earth and Environmental Sciences, Plymouth University, Plymouth, UK.*

Abstract

The cores of the fourteen Advanced Gas-cooled nuclear Reactors (AGRs) within the UK comprise Gilsocarbon graphite, a manufactured material surrounded predominantly by CO_2 at high pressure and temperature to provide heat exchange. The intense ionising radiation within the reactors causes radiolytic oxidation, and the resulting mass loss is a primary factor in determining reactor lifetime. The void structure of the porous Gilsocarbon graphite affects the permeability and diffusion of the carbon dioxide, and the sites of oxidation. To model this void structure, the porosities and densities of ten virgin Gilsocarbon graphite samples have been measured by powder and helium pycnometry. For comparison, results are also presented for highly ordered pyrolytic graphite (HOPG), and a fine-grained Ringsdorff graphite. Samples have been examined at a range of magnifications by electron microscopy. Total porosities and percolation characteristics have been measured by standard and cyclic mercury porosimetry up to an applied mercury pressure of 400 MPa. Inverse modelling of the cyclic intrusion curves produces simulated void structures with characteristics which closely match those of experiment. Void size distributions of the structures are presented, together with much Supplementary Information. The simulated void networks provide the bases for future simulations of the radiolytic oxidation process itself.

1. Introduction

Gilsocarbon graphite is used as a structural material and neutron moderator in the fourteen Advanced Gas-Cooled nuclear Reactors (AGRs) deployed in the UK. Gilsocarbon graphite is manufactured in several stages from Gilsonite pitch, a solid hydrocarbon bitumen mined from the Uinta Basin in Utah and Colorado. The first stage is to calcine the Gilsonite at 1300 °C which removes volatiles. The calcined coke is then ground and blended with a binder pitch, and the mixture moulded (pressed). Such moulding produces a semi-isotropic microstructure, which is assumed isotropic in this work. The material is then impregnated under vacuum with coal tar at high temperature to reduce the

*Corresponding author.
Email address: pmatthews@plymouth.ac.uk (G. Peter Matthews)

porosity and increase the density. Next the material is baked at 800 °C, re-impregnated and baked again. The product, Gilsocarbon, is then graphitised at a temperature approximately 2800 °C [1] to form moulded bricks of Gilsocarbon graphite which are then machined into octagonal blocks and keys which lock together to form the reactor core. Despite the impregnation, the final product nevertheless contains pores over a very wide range of sizes, as shown in Supplementary Information (SI) Figures 1 to 6. Each reactor contains around 675 t (metric tonnes) of Gilsocarbon graphite within its active core, and about 1500 t in total including the reflector and shield graphite.

Individual graphite layers are affected by intense neutron radiation, which causes changes in the dimensions and other material properties of the sample [1, 2]. The heat transfer in the reactors is carried out by CO_2 at high temperature and pressure, which exits the fule channels at around 620 °C and 4 MPa respectively. Within the active core at 460 °C, thermal oxidation is negligible [3]. However in the presence of intense ionising radiation within the active core, oxidative species can be produced, of uncertain identity, which can lead to oxidation of the Gilsocarbon graphite. While it is documented that CH_4 and other species can work as effective inhibitors to the radiolytic oxidation reaction, the chemistry of the process is not entirely understood [3]. The oxidation of Gilsocarbon graphite, and the consequent mass loss, is a primary limiting factor in the lifetime of the AGRs. Such lifetimes have become of great importance in the context of the desire further to extend the estimate of the safe working lifetimes of the UK's AGRs.

Studies suggest that the Gilsocarbon graphite microstructure has a significant effect on this radiolytic oxidation, with factors such as grain size, internal surface area and density having an effect on the oxidation rates [4]. The size and geometry of the pore network also affects radiolytic oxidation, since the pores act as gas transport channels [3, 5] and so will affect the permeability and diffusivity within the Gilsocarbon graphite. To aid the understanding and prediction of the rate of mass loss in Gilsocarbon graphite in AGRs, it is therefore of importance to generate a quantitatively realistic model of the void structure.

In order to develop such a quantitative model, inverse modelling of mercury intrusion porosimetry has been carried out, guided by porosities measured by pycnometry. Mercury porosimetry has the advantage of probing several orders of magnitude of void size, in the range relevant to the oxidation processes, unlike, for example, X-ray tomography (CT) for which the resolution is too coarse, typically greater than 5 µm. It also incorporates information about the connectivity of the voids, whereas in other techniques, such as the image analysis of thin sections, connectivity has to be guessed from the putative overlap of voids between successively microtomed layers. However, porosimetry also has its drawbacks. With granular samples, such as carbon black, it is necessary to identify effects due to inter- and intra-particle intrusion, and disintegration of the particles [6]. For the present samples, which are not granular, there is still the fundamental problem that large voids which can only be entered by narrow necks (throats) which shield them, register as narrow necks but with larger volumes [3]. So the normal method of analysing the intrusion curve, which is to take its first derivative and equate that to the void size distribution, underestimates the sizes of the voids. As shown below, this is especially important in Gilsocarbon graphite, in which, because of the manufacturing process, narrow necks shield much larger pores. A method is therefore needed to estimate this shielding effect. The

PoreXpert software developed in the authors' research group does so by modelling the intrusion curve as an entire characteristic rather than simply its first derivative, and by incorporating additional information, such as the porosity and an initial typical throat to pore size ratio, with a Bayesian type of approach guided by a multi-dimensional simplex. Hence a much more accurate estimate of the network connectivity and void sizes can be made, which is crucial to the current development of a more quantitative model based on the chemical and physical processes reviewed by Best et al in 1985 [3].

Previous modelling studies on nuclear graphite have shown how irradiation causes dimensional changes and changes in Young's modulus, using finite element modelling [7, 8] or an empirical model [9, 10]. However, in order to develop an approach for the study of irradiated samples, in this work the focus is on the characterisation of the porous structure of virgin (unirradiated) Gilsocarbon graphite.

2. Experimental procedure

2.1. Materials

Virgin Gilsocarbon graphite samples were supplied by EDF Energy Nuclear Generation Ltd, Barnwood, Gloucester, UK. They were cut or trepanned from spare blocks destined for the Hartlepool, Hinkley Point B, Heysham B and Torness nuclear reactors, but not deployed. Samples were identified for example as 70 4 D 4, where, in order, 70 is the brick number, 4 is the vertical section of the brick (smaller numbers are higher in the brick), D is the quadrant from which the sample was taken, and the final 4 is the core number within the quadrant. Other samples were identified for example P37 E9E 324/1B, where, in order, P indicates the reactor Hinkley Point reactor 3, 3 stands for the sample channel, 7 is the vertical position in the channel, E9 indicates that it is enclosed pot 9, with E indicating the position in the pot. 324 is the production run number, 1 is the vertical section of the brick and B is the quadrant.

Ten Gilsocarbon graphite samples were studied, and for control and comparison purposes, also two other types of graphite. The first was Highly Ordered Pyrolytic Graphite (HOPG), SI Figure 7, which is considered to be graphite in the most ordered and pure form available. The second was Ringsdorff graphite, SI Figure 8, which is a pure fine-grained graphite.

2.2. Sample preparation

Initial mercury intrusion experiments on adjacent sub-samples cut from the same sample showed a wide variation in intrusion characteristics at low pressures, converging to consistent intrusion curves at higher pressures. This was attributed to edge effects, as further considered in the Discussion below. Consequently all of the samples were machined to cylinders of diameter ranging from 10 - 12 mm, using a tungsten carbide tool on a standard lathe. The samples were then cut to approximately 5 mm in length with a diamond saw. Finally the samples were washed with deionised water and dried for at least 24 hours at 120 °C.

2.3. Pycnometry

Helium and envelope pycnometry measurements were made on all samples under local ISO 9001:2008 protocols. Helium pycnometry was carried out using a Pycnomatic ATC pycnometer (Thermo Fisher Scientific, Italy) operating at a temperature of 20 °C ± 0.01 °C. Before analysis, all samples were degassed for a minimum of six hours at approximately 270 °C under vacuum to ensure that there was no residual moisture in the samples, and to ensure that the samples were completely dry. All samples were loaded into a sample chamber of approximately 7 cm^3 with a reference volume of approximately 20 cm^3. To measure the helium-accessible pore volume, the helium pressure was raised from ambient to 0.2 MPa. The instrument was set up with an equilibrium time of 30 seconds, and an equilibrium pressure difference between the sample and reference volumes set as less than 0.01 kPa.

Envelope (powder) pycnometry was carried out on the same samples using a GeoPyc 1360 pycnometer (Micromeritics Corporation, USA) to obtain the envelope volume. The procedure involves running a blank experiment using a flowing powder (DryFlo supplied by Micromeritics) in a sample chamber with a known diameter. The powder is compressed by a tightly fitting plunger, and the apparent volume of the chamber measured as the force on the plunger is increased. A corresponding experiment is then carried out with the sample in the chamber. Subtraction of the second characteristic from the first gives the envelope volume of the sample. Samples were brushed after the experiments to remove residual DryFlo.

2.4. Mercury porosimetry

Finally, the same samples were subjected to mercury porosimetry. The experiments were carried out with a PASCAL 140 and a PASCAL 440 mercury porosimeter (Thermo Fisher Scientific, Italy), allowing intrusion to be measured from just above vacuum to 400 MPa applied pressure. They were operated in a mode which allowed the mercury pressure to re-equilibrate when intrusion or extrusion was detected. Cyclic experiments were also carried out, in which the applied pressure was reduced and then increased again. Such experiments required the re-programming of the firmware of the instruments, in collaboration with Thermo Fisher. All mercury porosimetry analyses were performed using local ISO 9001:2008 standard operating procedures, which were more rigorous than those suggested by the manufacturer.

The pressure values were converted into pore diameters using the Laplace-Washburn equation:

$$d = -\frac{4\,\gamma\,cos\theta}{P} = -\frac{\alpha}{P} \tag{1}$$

where d is the pore diameter, γ is the interfacial tension between the solid matrix, mercury and vacuum and is assumed to correspond to a value of 0.48 N m^{-1}, θ is the contact angle as discussed below, P is the applied pressure (Pa), and $\alpha = 4\,\gamma\,cos\theta$.

3. Modelling

3.1. The void network simulator

PoreXpert[1] is a new software package developed at Plymouth for the construction of void networks by inverse modelling of percolation characteristics. It is the more powerful successor to Pore-Cor Research Suite[2], which has been used in previous studies to model the porous network and pore level properties of various materials, such as sandstones, soil, catalysts and paper coatings [11, 12, 13, 14]. The void structure of a porous material is represented as a series of identical interconnected unit cells with periodic boundary conditions. Since mercury gives no information about the precise shapes of voids, their shapes were approximated as cubic pores connected by narrower cylindrical 'throats'. Each unit cell comprises an array of $n \times n \times n$ pores $\{n \in \mathbb{Z} \mid 5 \leq n \leq 30\}$, equally spaced in a Cartesian cubic-close-packed array, providing unit cell volumes up to 27 times larger than for Pore-Cor.

The network model can generate structures with porosity, and percolation properties such as mercury porosimetry, water retention or porometry, closely matching experimental measurements. To achieve this match, the geometry of the network is adjusted by an eight-dimensional Boltzmann-annealed amoeboid simplex to give a close fit to an experimental percolation curve. The closeness of fit is represented by a distance parameter – which is the average percentage distance of an experimental point to the nearest simulated point on the percolation curve, on a graph in which the total range of the logarithmic pressure or size axis and the accessible porosity axis have both been normalised to 100%.

Five of the dimensions of the parameter space are defined by continuously variable parameters, namely throat skew, throat spread, pore skew, connectivity and correlation level. Throat spread (the 'fatness' of the throat size distribution) and throat skew (the asymmetry of the distribution) describe an Euler beta distribution, which encompasses Gaussian-like and Poisson-like types. Distributions that asymptote to zero at the maximum and minimum size are defined as unimodal. The Euler beta function also encompasses bimodal distributions, with most void sizes at the upper and lower extremes of the range d_{max} and d_{min} [13]. The pore skew parameter, which bulks up the volume of pores, compensates for the fact that the regular positional spacing of the features in the network, irrespective of size, often makes it difficult to achieve the correct experimental porosity. Connectivity is the average number of throats per pore, ranging from 0 to 6. A typical value when modelling natural samples is 3.5. The short-range size auto-correlation is quantified by the correlation level parameter, which can vary between 0, for a random structure, to 1 in which throats, and hence adjoining pores, are grouped into pre-determined loci according to their size [15].

Once the network structure with the closest possible fit to experimental porosity and percolation characteristics is generated, several pore-level properties of the simulated material can be modelled, including tortuosity, permeability and thermal conductivity. The flow of wetting and non-wetting fluid can also be modelled [11, 16, 12].

[1]PoreXpert is a registered trademark of PoreXpert Limited.

[2]Pore-Cor is a trademark of the Environmental and Fluid Modelling Group, Plymouth University.

3.2. The non-wetting fluid extrusion algorithm

A new algorithm for the simulation of the extrusion of non-wetting fluid when the external pressure is progressively reduced was developed in order to simulate the experimental results obtained by cyclic mercury porosimetry. In order to understand it, some principles of mercury extrusion must first be comprehended.

Eq.1 predicts that a cylinder of diameter d will be intruded by mercury at an applied pressure equal or greater than P. Suppose that at the end of an intrusion process, the local geometry of the cylinder is such that the shape of the meniscus, and its associated line force at the phase interface, is retained. Then if the pressure P is reduced, the mercury will be extruded back out of the capillary tube by the meniscus force. If the pressure is increased once again, there will be no hysteresis, Figure 1a. In practice however, the intruding and extruding contact angle can change by up to 30° [17]. In the present extrusion algorithm, typical contact angle values are used, 140° for the advancing (intruding) contact angle, and 130° for the receding contact angle [18]. Such hysteresis is fully reversible, Figure 1b, provided that the intrusion and extrusion process does not progressively change the nature of the surface of the cylindrical void.

Suppose that mercury is forced through a narrow entry channel, or 'throat', on the downstream side of which is a large void. For a throat of diameter diameter d_{throat} , such intrusion requires a pressure $-\alpha/d_{\text{throat}}$ according to Eq. 1, which is also sufficient to intrude the larger shielded void of diameter d_{pore}. However, for the mercury to be withdrawn (extruded) again, the pressure must drop below $-\alpha/d_{\text{pore}} < -\alpha/d_{\text{throat}}$. Hence there is hysteresis, Figure 1c. Additionally, micro-model experiments by Wardlaw [19] and others have shown that for $d_{\text{pore}} \gtrsim 5d_{\text{throat}}$ the mercury column 'snaps off' and the mercury in the pore remains trapped. This condition is more likely to be satisfied by pores that only have one entrance, known as 'ink-bottle-pores' [20]. For a structure in which all pores satisfy the condition $d_{\text{pore}} \gtrsim 5d_{\text{throat}}$ there is complete trapping, and contact angle hysteresis become irrelevant because there is no extrusion, Figure 1d. Such behaviour also occurs when mercury intrudes cracks through a small entry channel.

A detailed algorithm for the simulation of non-wetting fluid extrusion from the simulated porous network would require, for each decreasing pressure step and for each node of the structure (pore), a full mapping of the possible paths going from the node to the sink where the non-wetting fluid is collected. However, these calculations would be extremely complex to implement and very time consuming. The simpler approach taken in this study is to assume that the throats on the top surface of the PoreXpert unit cell are connected to a mercury sink. Initially the algorithm identifies the pores in which snap-off is going to occur. These are the pores that have only one large entry throat while all the remaining throats have diameter smaller than the pore size divided by the snap-off ratio (taken to be 5). Once this list of pores has been fully defined the algorithm will loop through the values of applied pressure. The pressure applied onto the mercury is progressively reduced and a pore is emptied out if: (i) its diameter is smaller than the corresponding Laplace diameter for the current value of external pressure, and (ii) it is connected to at least another pore which is not in the list of pores for which snap-off occurs.This is an approximation of the extrusion process; instead of taking into account all the possible routes for the mercury to take from one pore to the sink, our analysis is limited to 2 adjacent pores. An algorithm in the preceding Pore-Cor software was

based on a similar level of approximation, and a sensitivity analysis suggested that although this level of approximation precludes the modelling of the precise shape of the extrusion curve, nevertheless it should provide a useful indication of the general level of trapping [21].

4. Results

4.1. Pycnometry

The results from the pycnometry experiments are listed in the first six of the eight columns of Table 1. Repetitions of the pycnometry measurements were made on the same sample, and the table shows the average results and instrumental relative standard deviations (RSDs) of the measurements. Also shown at the bottom of the Table are the means and RSDs across the ten samples . It can be seen that the densities are similar, with a mean of 2.138 g cm^{-3} and RSD of 2.8%. As expected, these are lower than the theoretical density of 2.26 g cm^{-3}. However, the helium accessible porosities ϕ_{He} varied widely around the mean value of 10.59%, with a RSD of 32.3%.

4.2. Mercury porosimetry

Standard non-cyclic porosimetry curves were first measured for all samples, as presented in the Supplementary Information (SI), Figures 9 to 18. Results for the two control samples, Ringsdorff graphite and grade A Highly Ordered Pyrolytic Graphite (HOPG), are shown in SI Figure 19 and SI Figure 20 respectively.

The extent of intrusion of mercury at the highest pressure (400 MPa) gave a lower bound to the total porosity of each Gilsocarbon graphite sample. Since the intrusion was still continuing at that pressure, the total porosities ϕ_{tot} are higher than those shown as $\phi_{\mathrm{tot}}^{\mathrm{min}}$ in Table 1. The Table also shows the closed porosities, $\phi_{\mathrm{c}}^{\mathrm{min}} = \phi_{\mathrm{tot}}^{\mathrm{min}} - \phi_{\mathrm{He}}$. Since the total porosity is a minimum bound, then these closed porosities are also minimum bounds - i.e. they are in fact higher than those shown.

Regions of interest on the non-cyclic curves were those in which the change of intrusion with pressure tended to a maximum (step) or minimum (plateau). Pressure ranges were chosen for cycling, identical for all samples, which would probe these regions, SI Table 1. As expected, all the cyclic porosimetry curves had the same outline shape as the non-cyclic curves. An example of a cyclic porosimetry curve is given in Figure 2.

All of the mercury intrusion curves have been corrected by subtracting the result of a blank experiment - i.e. an experiment carried out with the same pressure settings but with no sample in the sample chamber. This procedure corrects for any minor void features in the sample chamber which may themselves be intruded, the expansion or contraction of the sample chamber, and the compression, rather than intrusion, of the sample and the mercury. Such a correction is inexact for a cyclic curve, because these physical processes do not replicate exactly between the sample run and blank, and small artefacts can arise. An example of such an artefact is the cyclic loop at the highest cycling pressure (150 MPa) in Figure 2. The extrusion part of the loop indicates that intrusion at first increases as the pressure is decreased, which is physically impossible. A similar artefact is frequently seen in experiments in which

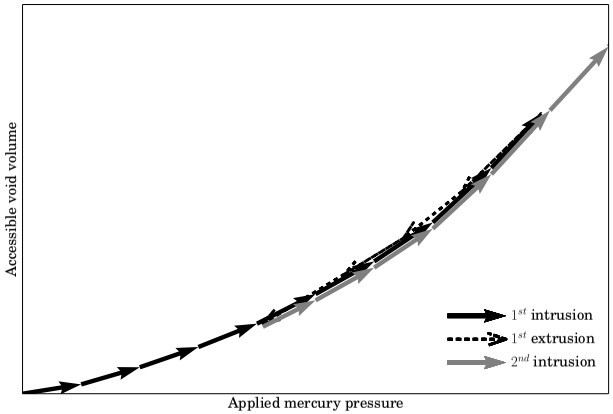

(a) no trapping and no contact angle hysteresis.

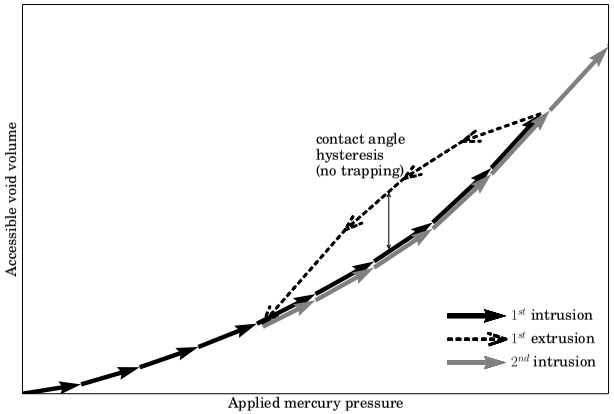

(b) contact angle hysteresis.

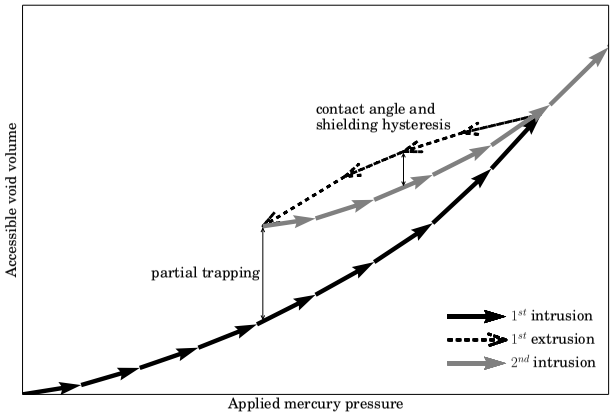

(c) contact angle hysteresis and partial trapping.

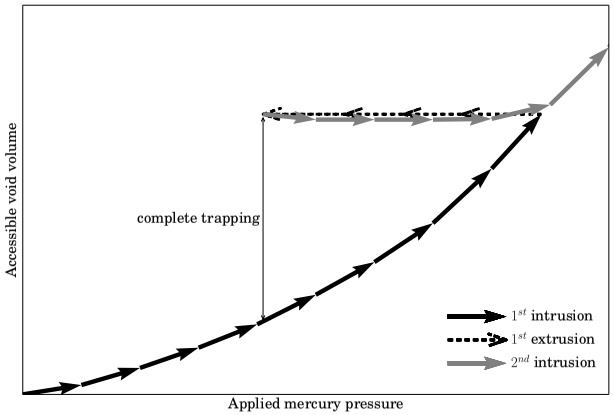

(d) complete trapping.

Figure 1: mercury intrusion-extrusion cycles.

Table 1: Gilsocarbon graphite densities derived from powder and helium pycnometry, and porosities derived from pycnometry and mercury porosimetry, showing instrumental and sample relative standard deviations (RSDs). The average envelope density has been measured by powder pycnometry and average density by helium pycnometry. Group A, as explained in the text, above the line, and Group B below.

Sample	Average envelope density / g cm^{-3}	Instrument RSD / %	Average density / g cm^{-3}	Instrument RSD / %	Helium accessible porosity, ϕ_{He} / %	Minimum closed porosity, ϕ_c^{min} / %	Minimum total porosity, ϕ_{tot}^{min} / %
62 2 C 10	1.8797	0.36	2.1715	0.24	13.44	3.92	17.36
70 4 D 4	1.9204	0.84	2.2033	0.38	12.83	3.35	16.18
8 C 5 2	1.8494	0.54	2.1620	0.48	14.46	7.52	21.98
P37E5A 540 3A	1.8773	0.25	2.1537	0.14	12.83	4.95	17.78
P37E9E 324 1B	1.8506	0.77	2.1609	0.34	14.36	6.20	20.56
P37E5C 921 2A	1.9405	0.42	2.0855	0.12	6.95	11.02	17.97
62 4 D 4	1.9048	1.14	2.0422	0.01	6.74	11.28	18.02
62 6 D 4	1.9187	0.73	2.0690	0.08	7.27	17.16	24.43
70 2 D 6	1.9744	0.57	2.1059	<0.01	6.25	9.82	16.07
70 6 D 10	1.9871	0.56	2.2268	0.12	10.77	10.26	21.03
Mean	1.9103	0.62	2.1381	0.19	10.59	8.55	19.14
Sample RSD/ %	2.5		2.8		32.3	49.4	14.3

the mercury has been intruded too quickly and has consequently been heated by the rapid increase in pressure - but in all the current experiments, it was ensured that mercury intrusion was slow.

Also shown in Figure 2 is the helium-accessible volume measured by pycnometry, measured at a helium pressure of 0.2 MPa. It can be seen that the accessible void volume measured by the helium at 0.2 MPa corresponds to that accessible by Hg at around 60 MPa - a difference in pressure of more than two orders of magnitude. It was found that Figure 2 represents one class of behaviour in the samples studied, referred to as Group A, in which the pycnometry void volume corresponds to the mercury intruded volume some way up the high pressure (nanoporosity) step. Samples in this group are shown in the top part of Table 1. A second group of samples, Group B, displayed a more sloping mercury intrusion plateau, with the pycnometry volume corresponding to the bottom of the slope at around 0.2 MPa, for example as shown in SI Figure 22. These are shown in the lower part of Table 1. It can be seen that these two groups did not divide by brick i.e. parts of the same brick behaved in two different ways.

To reconcile the difference between the He-accessible and Hg-accessible porosities, two assumptions are made. For Group A, in which the He accessible porosity corresponds to the Hg intrusion at around 60 MPa, the entire open porosity of these structures, as measured by pycnometry, can be accessed by the mixture of gases present in the nuclear reactor. Therefore for modelling purposes it is reasonable to assume that the relevant void space for an AGR is represented by the Hg intrusion up to 60 MPa.

For group B, the He-accessible porosity corresponds to a pressure below that in an AGR (4 MPa). However it is assumed that the gases in the nuclear reactor should be able to partially open the void structure, and access the same void volume accessed by mercury at 4 MPa. These different truncations of the cyclic intrusion curves for Group A and Group B are applied in Figures 6 to 9. Other cyclic intrusion curves are presented in SI Figures 21 to 30.

The cyclic curve for one of the controls, Ringsdorff, is shown in Figure 5. Unlike the non-cyclic curve, SI Figure 19, this shows a step at low pressures. In normal non-cyclic mode, the PASCAL 140 porosimeter allows two successive low pressure cycles to be carried out before a single high pressure cycle. By doing this, inter-particle intrusion, apparent only during the first low pressure cycle, is discarded. Only the second low pressure cycles are shown in SI Figures 9 to 18. In the cyclic curves, all cycles are shown in full, with the first showing inter-particle intrusion.

4.3. Modelling

The network modelling software was used to generate simulated porous structures from the intrusion curves of four samples, truncated as described above: two from Group A (62 2 C 10 and P37E9E) and two from Group B (62 4 D 4 and 70 6 D 10). The fitting parameters are listed in SI Table 2. A unit cell of one of the resulting structures, in which the solid phase is shown transparent and the voids as solid, is shown in Figure 3. Mercury (dark grey) has been intruded to 51.4% by volume by applying a pressure of 0.17 MPa. Once generated, the structure can be interrogated to give properties such as the size distribution of pores and throats, shown in Figures 4a to 4d. Note that both axes are logarithmic - the distributions cover a very wide size range and are very highly bimodal. The distributions bear no relationship to those derived

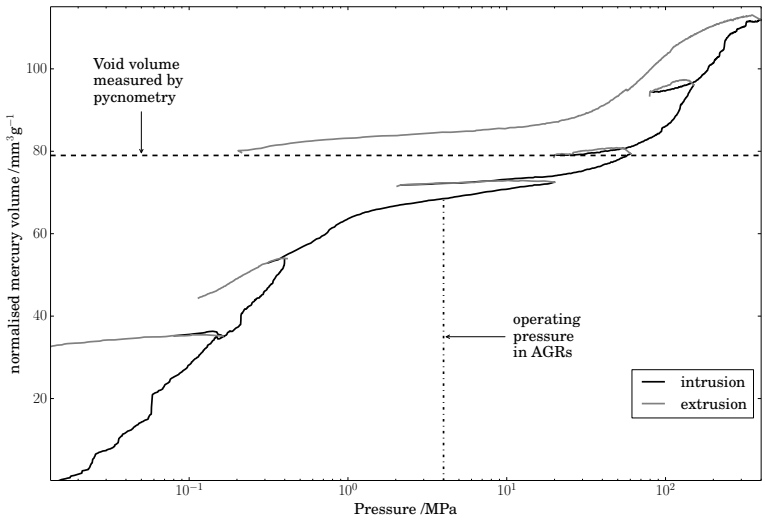

Figure 2: full cyclic mercury porosimetry curve for sample P37E9E, with the equivalent pycnometry void volume identified and operating pressure of AGR (4 MPa).

from the traditional analysis of mercury intrusion curves, which is simply to take the gradient of the curves - a process which implicitly assumes that the void structure comprises a bundle of aligned, differently sized capillary tubes.

Cyclic intrusion curves, based on structures such as that shown in Figure 3, were simulated by applying the non-wetting fluid intrusion and extrusion algorithms in cycles with the same table of pressures used experimentally, SI Table 1.

There is close agreement between the experimental and simulated cyclic porosimetry results, as shown in Figures 6 to 9. It might be suspected that the approximations described in the second part of section 3.2 cause there to be total trapping and no extrusion within the simulation. However, it can be seen in Figure 7 that there is some extrusion of mercury both experimentally and in the simulation, for the cycle starting at 0.2 MPa.

5. Discussion

Before making conclusions about the structure of Gilsocarbon graphite, one should first consider the intrusion curves of the control samples. SI Figure 20 shows that mercury barely intrudes HOPG; the slight observed porosity of 1.17% can be attributed to intrusion of surface defects. The Ringsdorff intrusion, by comparison, shows in Figure 5 an initial step due to inter-granule intrusion, and a major step due to inter-feature intrusion. The features in question, creating a porosity of at least 11.6%, SI Figure 19, are visible in SI Figure 8. There is also steadily increasing intrusion at pressures above 10 MPa. The cause of this increasing intrusion at high pressures is difficult to identify - it may arise from distortion of the graphite layered structure to reveal previously hidden voids.

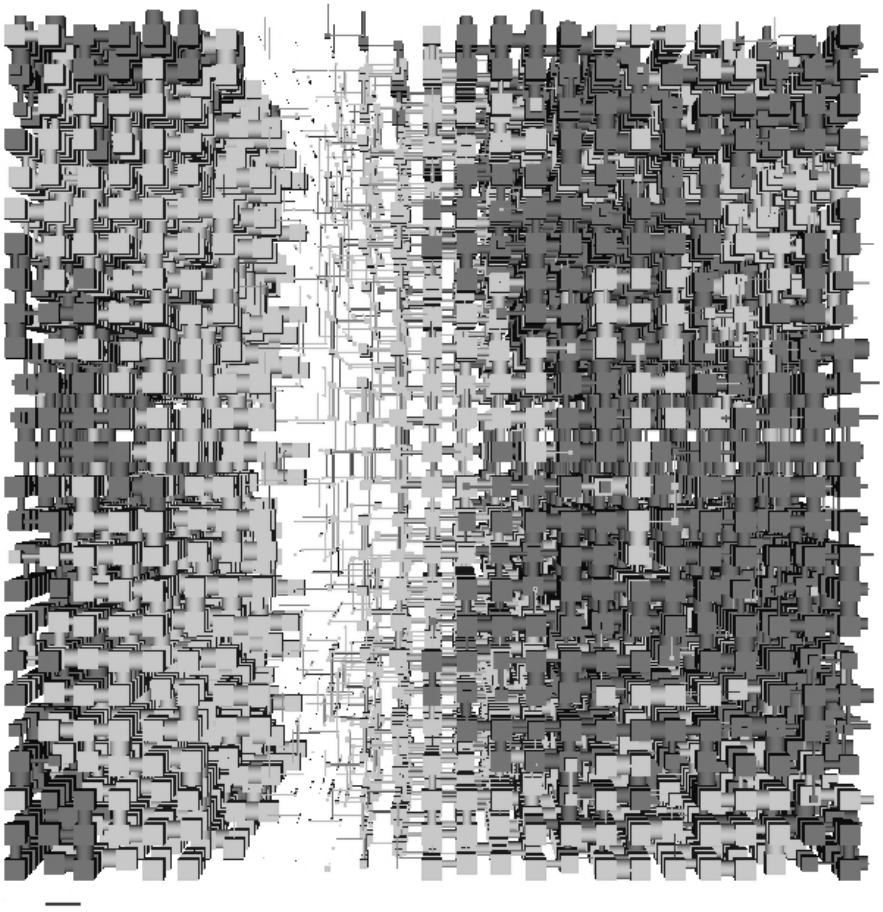

Figure 3: PoreXpert unit cell for sample P37E9E. The small bar bottom left has length 164.8 µm. The void features cover four orders of magnitude in size, so many are invisibly small in the figure. The white / transparent region corresponds to the solid Gilsocarbon graphite matrix. The void features are grey with dark grey indicating the presence of mercury.

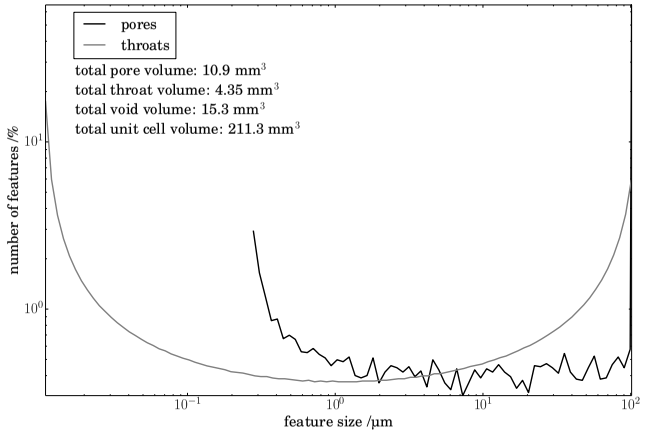

(a) sample 62 2 C 10.

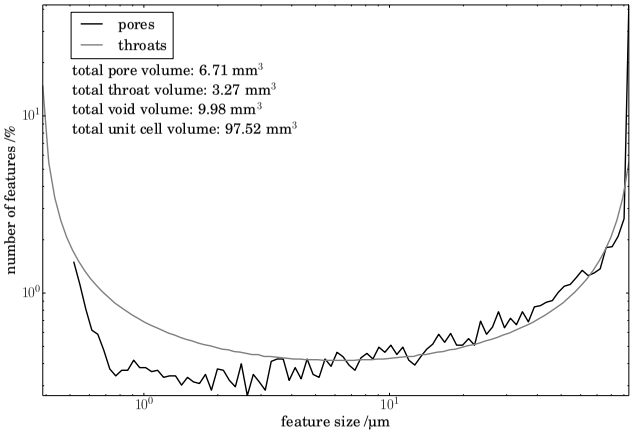

(b) sample 62 4 D 4.

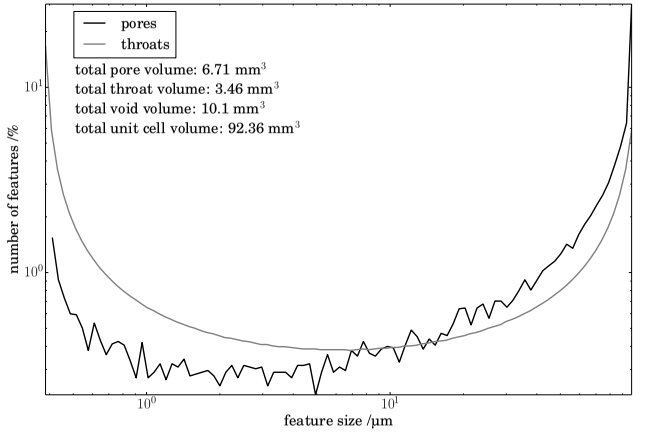

(c) sample 70 6 D 10.

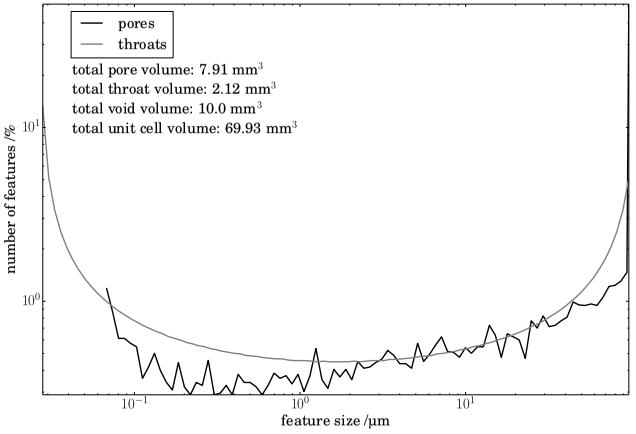

(d) sample P37E9E.

Figure 4: simulated pore and throat size distributions.

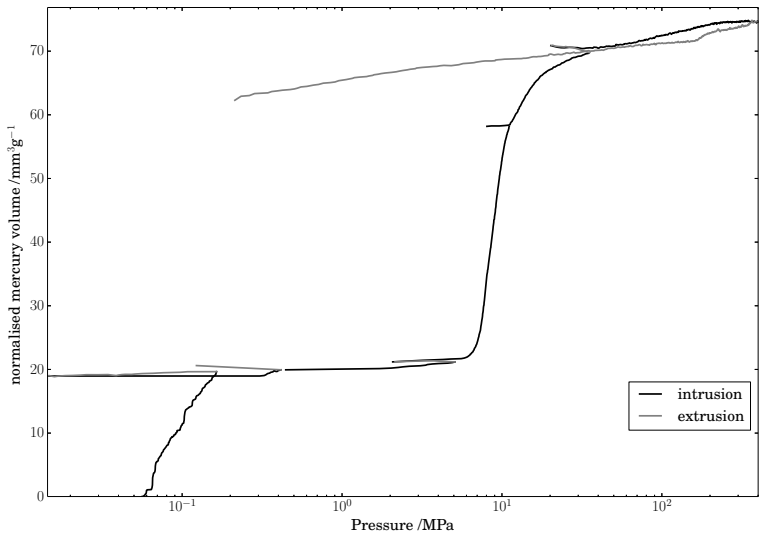

Figure 5: experimental cyclic mercury porosimetry for Ringsdorff graphite.

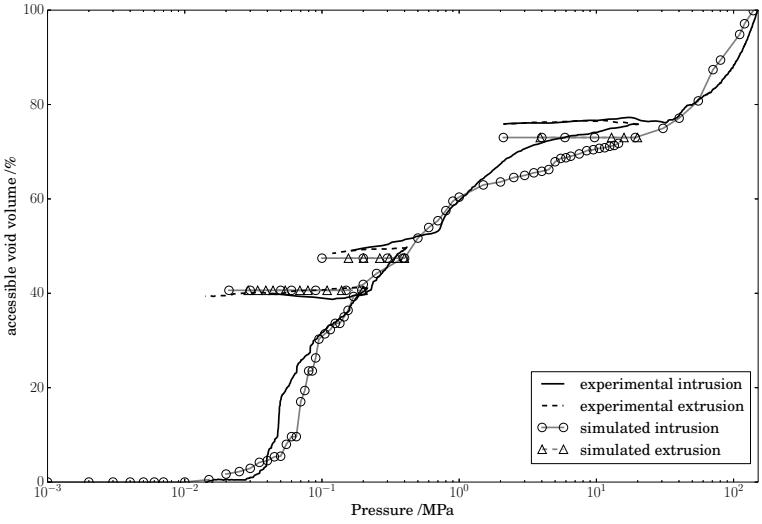

Figure 6: experimental and simulated cyclic mercury porosimetry for sample 62 2 C 10.

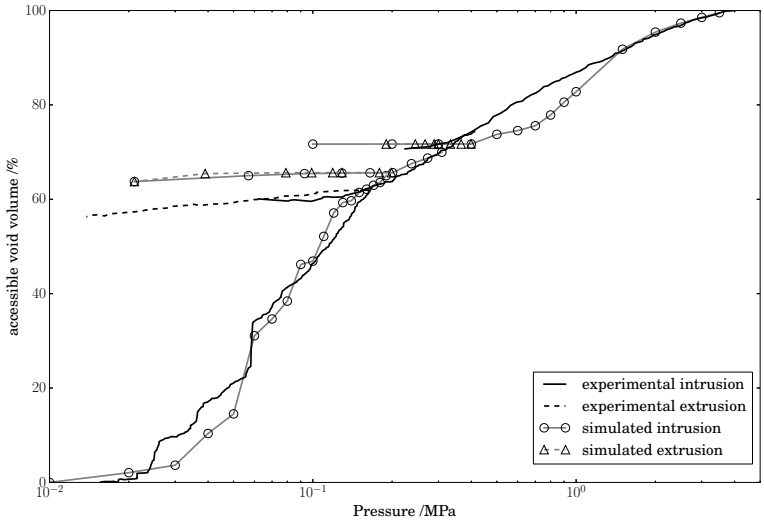

Figure 7: experimental and simulated cyclic mercury porosimetry for sample 62 4 D 4.

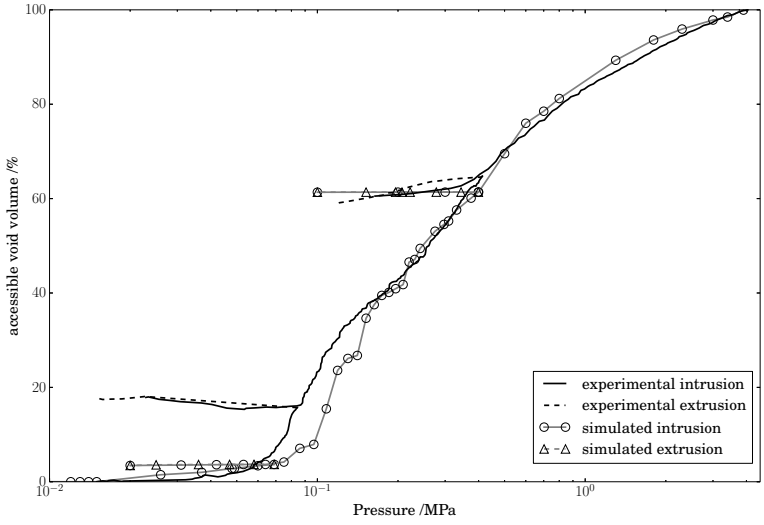

Figure 8: experimental and simulated cyclic mercury porosimetry for sample 70 6 D 10.

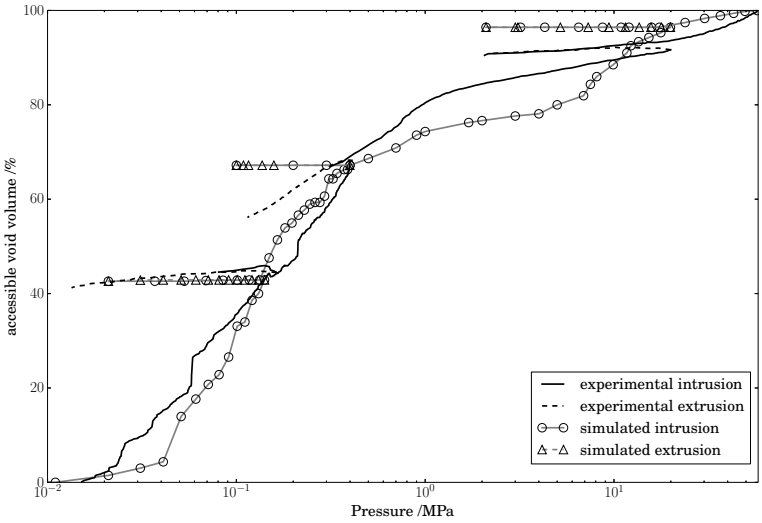

Figure 9: experimental and simulated cyclic mercury porosimetry for sample P37E9E.

Moving our attentions to Gilsocarbon graphite, it is possible to see that there is progressive intrusion both at low and high pressure, SI Figures 9 to 18. This is readily explained by the complexities of the void structure visible at every level of scale, SI Figures 1 to 6. However, these images give no basis for assuming that the structure is generally fractal, despite inferences from SANS measurements at scales below 500 nm [22]. At high pressure, the intrusion effect is likely to be the same as that observed in Ringsdorff graphite. Sample compression can be discounted, because the apparent intrusion and extrusion curves generated solely by elastic compression of a sample show no hysteresis at high pressures, Figure 1a. With regard to the cyclic curves, the simulation predicts, *a priori* on the basis of the intrusion curve and sample porosity, that total or almost total trapping occurs over the whole intrusion pressure range (and hence for every size) , as shown in Figure 1d. In the present case, it has done so because it has generated a void network in which nearly all of the pores are more than 5 times larger than their adjoining throats in the intrusion/extrusion direction, and which therefore trap all of the mercury, Section 3.2. However, such behaviour would also have been observed had the model been anisotropic and thus able to generate cracks. Such behaviour is not seen in natural samples such as sandstones, which usually show the characteristics shown in Figure 1c. The oddity of behaviour in Gilsocarbon graphite can be explained by its manufacture, described in Section 1. The application of coal tar pitch and the subsequent graphitisation process cause the entries into the void networks to be blocked up, or almost blocked up, by graphitised coal tar pitch at the entrance to each network. Mercury enters through the residual opening, which is much smaller than the original throat, and even smaller relative to the pores shielded by the throat. Therefore no mercury retracts on reducing the pressure. In practice the situation is complicated by the fact that after impregnation and during baking, gases are released that form voids in the binder phase. These

voids may have small entries through which the gas vents, or have a narrow wall through which mercury can break as the applied mercury pressure increases during porosimetry. Then on graphitisation Mrozowski cracks are formed both in the filler and binder phase, which themselves can give rise to total trapping of intruded mercury.

These considerations point to two weaknesses of the model. The first is its simplified, isotropic geometry. Mercury intrusion gives no information about the shape of the voids - only their cross-sectional areas, volumes and connectivity. Therefore the model simplifies their shapes to isotropic cylinders and cubes, with no ability to represent anisotropic Mrozowski cracks. Taking the intrusion curve as a whole yields some information about the short-range size auto-correlation between void features. In Figure 3 , it can be seen that the voids are correlated in vertical layers - i.e. layers parallel to the direction of mercury injection from the top surface. However, no further information can be extracted from the intrusion characteristic about the existence of localised structures such as the small 'onion ring' concentric slits that are often observed [3].

The second weakness of the model is that it is based on the shape of the whole intrusion curve up to the point of truncation, as a representation of a single, static void structure of the sample. It does not model any progressive breakthrough by mercury into closed porosity as the applied pressure is increased, for example into that due to trapped gas bubbles. That such progressive breakthrough does occur is supported by the very high variability of low pressure intrusion curves if samples are not prepared in a standard fashion, Section 2.2. It is also supported by the difference in behaviour between groups A and B, described above. Additional corroboration is given by small angle neutron scattering (SANS) experiments on irradiated Gilsocarbon graphite, in which closed porosity was measured by soaking the samples in D-toluene as a contrast-matching fluid [22]. The experiments showed a closed porosity of around 30% of total porosity in the size range 0.2 to 300 nm - i.e. smaller than the 4 nm to 100 µm range studied in this work. It compares with our average result, from Table 1, of 8.55 / 19.14 = 44.7%. Since the total and closed porosities are not independent, the RSDs of the ratio sum in quadrature, and the resultant RSD is 51.4%. Our results and the SANS result therefore agree within one standard deviation.

Another feature of this second weakness is that changes within the structure induced by the increasing applied mercury pressure are not modelled. On stressing graphitic structures at the micro- and nano- scale, they can deform due to processes such as "twinning" and kinking, and such processes may reverse on reduction of the applied pressure [23]. These processes, if present, could cause the voids to close and open, thus influencing the mercury intrusion and extrusion characteristics. However, since the micro- and nano-structure of the sample cannot be monitored whilst it is immersed in mercury, these processes cannot be modelled.

As mentioned above, a likely source of at least some of the closed porosity is gas bubbles trapped during manufacture, probably CO and N_2. In other previous work [3], it was explained why such closed porosity will not provide sites for radiolytic oxidation in an AGR until they are made accessible to the circulating CO_2 by gas pressure, or by progressive mass loss of the surrounding solid phase. In the same previous work, a sample of virgin Gilsocarbon graphite was pressurised up to 100 MPa in ethanol, which was then evaporated out again.

This procedure made no difference to the subsequent mercury intrusion curve. Such behaviour can be explained as similar to Group A of our samples - i.e. with most of the porosity accessible.

6. Conclusions and future work

Pycnometry results have shown that while the density of our ten Gilsocarbon samples was very constant, the He, closed and total porosities varied widely. The electron micrographs and mercury intrusion measurements presented in this work and its accompanying electronic supplementary information have confirmed that the void structure of Gilsocarbon graphite is complex at every size level. Simulated void structures, over four orders of magnitude of size, have been generated with percolation characteristics which closely match experimental pycnometry and cyclic mercury intrusion measurements. Inverse modelling of the mercury intrusion characteristics produces a much more realistic estimate of the void sizes than has been available previously, and provides the basis for a quantitative estimate of the rate of oxidation, and hence mass loss, in Gilsocarbon graphite under intense ionizing radiation.

Although this study has been carried out on virgin graphite, truly useful insights can only be gained by a similar study on samples which have been subjected to high neutron flux, and have thus undergone the changes in dimension and material properties cited in Section 1. Preparation for such work is currently under way.

Acknowledgements

The financial support and advice of EDF Energy (Barnwood, Gloucester, UK) is gratefully acknowledged. However the views expressed in this paper are those of the authors and do not necessarily represent the views of the sponsors. The firmware re-programming was carried out for us by CAD92 di Tacconi Roberto, 20096 Pioltello MI Italy. The authors are grateful for the advice of Anthony Wickham, Visiting Professor in the School of Mechanical, Aerospace and Civil Engineering, University of Manchester, UK. The authors would also like to thank the University of Plymouth Electron Microscopy Centre, and finally Dr. Luca Lucarelli of Thermo Fisher Scientific (Rodano, Milano, Italy) for collaborating on the development of the custom PASCAL mercury porosimeter firmware.

Appendix A. Supplementary materials

Supplementary data associated with this article can be found in the on-line version at ...

References

[1] B. J. Marsden, G. N. Hall, O. Wouters, J. Vreeling, J. van der Laan, Dimensional and material property changes to irradiated Gilsocarbon graphite irradiated between 650 and 750°C, J. Nucl. Mater. 381 (1-2) (2008) 62–67.

[2] A. N. Jones, G. N. Hall, M. Joyce, A. Hodgkins, K. Wen, T. J. Marrow, B. J. Marsden, Microstructural characterisation of nuclear grade graphite, J. Nucl. Mater. 381 (1-2) (2008) 152–157.

[3] J. V. Best, W. J. Stephen, A. J. Wickham, Radiolytic Graphite Oxidation, Prog. Nucl. Energy 16 (2) (1985) 127–178.

[4] P. Wang, C. I. Contescu, S. Yu, T. D. Burchell, Pore structure development in oxidized IG-110 nuclear graphite, J. Nucl. Mater. 430 (1-3) (2012) 229–238.

[5] M. S. El-Genk, J.-M. P. Tournier, Development and validation of a model for the chemical kinetics of graphite oxidation, J. Nucl. Mater. 411 (1-3) (2011) 193–207.

[6] R. Pirard, B. Sahouli, S. Blacher, J. Pirard, Sequentially Compressive and Intrusive Mechanisms in Mercury Porosimetry of Carbon Blacks., J. Colloid Interface Sci. 217 (1) (1999) 216–217.

[7] G. Hall, B. J. Marsden, S. L. Fok, The microstructural modelling of nuclear grade graphite, J. Nucl. Mater. 353 (1-2) (2006) 12–18.

[8] C. Berre, S. L. Fok, B. J. Marsden, P. M. Mummery, T. J. Marrow, G. B. Neighbour, Microstructural modelling of nuclear graphite using multi-phase models, J. Nucl. Mater. 380 (1-3) (2008) 46–58.

[9] E. D. Eason, G. N. Hall, B. J. Marsden, G. B. Heys, A model of Young's modulus for Gilsocarbon graphites irradiated in oxidising environments, J. Nucl. Mater. 436 (1-3) (2013) 201–207.

[10] E. D. Eason, G. N. Hall, B. J. Marsden, G. B. Heys, Models of coefficient of thermal expansion (CTE) for Gilsocarbon graphites irradiated in inert and oxidising environments, J. Nucl. Mater. 436 (1-3) (2013) 191–200.

[11] P. Bodurtha, G. P. Matthews, J. P. Kettle, I. M. Roy, Influence of anisotropy on the dynamic wetting and permeation of paper coatings, J. Colloid Interface Sci. 283 (2005) 171–189.

[12] G. P. Matthews, C. Canonville, A. K. Moss, Use of a void network model to correlate porosity, mercury porosimetry, thin section, absolute permeability and NMR relaxation time data for sandstone rocks, Phys. Rev. E 73 (2006) art 031307.

[13] G. P. Matthews, G. M. Laudone, A. S. Gregory, N. R. A. Bird, A. G. Matthews, W. R. Whalley, Measurement and simulation of the effect of compaction on the pore structure and saturated hydraulic conductivity of grassland and arable soil, Water Resour. Res. 46 (5) (2010) W05501.

[14] G. M. Laudone, G. P. Matthews, A. S. Gregory, N. R. A. Bird, W. R. Whalley, A dual-porous, inverse model of water retention to study biological and hydrological interactions in soil, Eur. J. Soil Sci. 64 (2013) 345–356.

[15] J. C. Price, G. P. Matthews, K. Quinlan, J. Sexton, A. G. D. Matthews, A Depth Filtration Model of Straining within the Void Networks of Stainless Steel Filters, AIChE J. 55 (12) (2009) 3134–3144.

[16] G. P. Matthews, Computer modelling of fluid interactions in porous coatings and paper - an overview, Nord. Pulp Pap. Res. J. 15 (5) (2000) 422–430.

[17] C. L. y. León, New perspectives in mercury porosimetry, Adv. Colloid Interface Sci. 76-77 (1998) 341–372.

[18] J. van Brakel, S. Modry, M. Svata, Mercury Porosimetry: State of the Art, Powder Technol. 29 (1981) 1–12.

[19] N. C. Wardlaw, M. McKellar, Mercury Porosimetry and the Interpretation of Pore Geometry in Sedimentary Rocks and Artificial Models, Powder Technol. 29 (1981) 127–143.

[20] Q. Zeng, K. Li, T. Fen-Chong, P. Dangla, Analysis of pore structure, contact angle and pore entrapment of blended cement pastes from mercury porosimetry data, Cem. Concr. Compos. 34 (9) (2012) 1053–1060.

[21] G. P. Matthews, C. J. Ridgway, M. C. Spearing, Void Space Modeling of Mercury Intrusion Hysteresis in Sandstone, Paper Coating, and Other Porous Media, J. Colloid Interface Sci. 171 (1) (1995) 8–27.

[22] Z. Mileeva, D. Ross, S. King, A study of the porosity of nuclear graphite using small-angle neutron scattering, Carbon 64 (2013) 20–26.

[23] P. Heard, M. Wootton, R. Moskovic, P. Flewitt, Deformation and fracture of irradiated polygranular pile grade A reactor core graphite, J. Nucl. Mater. (1-3) 223–232.